



**Politecnico
di Torino**



**Université
Paris Cité**

Université Paris Cité
Lab: Matériaux et Phénomènes Quantiques (MPQ)
Group: Dispositifs Optiques Non-linéaires (DON)

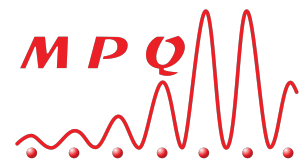
Master Thesis

M2 - Quantum Devices
Double Degree Program NanoQuad

Sum frequency generation in AlGaAs-based nonlinear waveguides

CANDIDATE
Luca LOVISOLO

SUPERVISOR
Pr. Giuseppe LEO



Paris
June, 2022

Acknowledgements

I would like to thank Giuseppe Leo for for accepting me in the DON group.

A special thanks to Andrea Gerini who followed and trained me throughout my internship. Thanks to Giulio Tavani for all the time spent together. I share with him many of the results presented in this work.

I would like to thank all the members of the team, always open for clarifications: Marco, Vincent, Laure and all the others.

Thanks to all my NanoQuad colleagues with whom I spent a wonderful year in Paris: Marco, Luca, Andrea, Giorgio, Gregorio, Valerio, Gaia, Eduardo, Ivan.

A special thanks to my family that supported me in all my decisions and difficult times.

Contents

Table of Contents	2
0.1 Introduction	3
1 Brief introduction on nonlinear optics	4
1.1 Propagation of the electromagnetic field into a waveguide	6
2 Design of the device	8
2.1 Low-contrast waveguides	9
2.1.1 Design of the straight waveguide	9
2.1.2 Design of the arc-shape waveguide	14
2.1.3 Tunability of the entire structure	17
2.2 High-contrast waveguides	20
2.2.1 Arc-shape waveguide and tunability	23
2.2.2 Fabrication of high-contrast waveguides	24
2.3 Conclusion	25
3 Reference articles	27

0.1 Introduction

Since the demonstration of second-harmonic generation (SHG) in 1961, nonlinear optics has been an important branch of optics research. Generation of new optical frequencies is indeed a powerful tool that has been widely used for many applications: it enables a huge array of capabilities in optical signal generation and processing, such as switching and demultiplexing of signals, radio-frequency spectroscopy. In quantum computing and quantum communication, non linear optics components are often used for the generation of entangled photon pairs or to convert single photons to telecommunication wavelengths. This huge variety of applications motivates the creation of efficient nonlinear optical components with photonic integrated circuits reducing the footprint.

Among all the applications, the area of research on mid-infrared detector for gas sensing has is huge interest. The mid-infrared (mid-IR) region of the optical spectrum is an important range for applications in gas sensing and integrated nonlinear photonics offers the best outlook for achieving these functions at low cost, while maintaining good performance. Gas molecules vibrational motion radiates light in the mid-infrared spectrum. State of the art mid-infrared detectors, however, are not on-chip integrable, require cryogenic temperatures and are quite expensive. Nonlinear optics allows to convert a mid-infrared wave into a near-infrared that can be easily detected with standard silicon photodiodes, which are compact and cheap.

In this work I will present the design of a device for the up-conversion of a mid-infrared signal into a near-infrared signal by means of a pump. The device concept is a long waveguide that takes advantage of the second-order optical susceptibility of the core media. Indeed guided-wave nonlinear optics has arisen research interest since the earliest stage of integrated optics. Second-order nonlinear effect have been studied with various waveguides materials and phase matching schemes. Materials considered includes ferroelectric crystals such as LiNbO_3 , organic crystals, and III-V semiconductors. Among all materials available, Aluminum Gallium Arsenide is a favorable one for up-conversion device because of its large quadratic nonlinear optical coefficients and well-established processing technology. AlGaAs waveguides have allowed the achievement of important results in terms of tunable sources or quantum optics and information

This work has been done in the laboratory Matériaux et Phénomènes Quantiques (MPQ) in the Dispositif Optiques Nonlinéaires group (DON), where the main research concern nonlinear optics phenomena, optomechanics and optoelectronics. The first topic is the field of study of my supervisor, Giuseppe Leo, whose research mainly focuses on AlGaAs nonlinear nanophotonics and nonlinear metasurfaces.

Chapter 1

Brief introduction on nonlinear optics

The term "nonlinear optics" refers to those phenomena that occur when the response of a medium to electric field depends in a nonlinear way on the strength of that. Those phenomena occur when the optical properties of a material depends on light intensity. The induced polarization \mathbf{P} can be written as:

$$P_i = \epsilon_0 \left(\sum_j \chi_{ij}^{(1)} E_j + \sum_{jk} \chi_{ijk}^{(2)} E_j E_k + \sum_{jkl} \chi_{ijkl}^{(3)} E_j E_k E_l + \dots \right) \quad (1.1)$$

where $\chi^{(2)}$ and $\chi^{(3)}$ are known as the second- and third-order nonlinear optical susceptibility tensor, respectively. The reason why the polarization plays a key role in the description of nonlinear optical phenomena is that a time-varying polarization $\mathbf{P}(t)$ can act as a source of new components of the electric field. In this report I will focus only in the second-order nonlinear processes. It is important to note that the tensor $\chi^{(2)}$ is non-zero only for non-centro symmetric materials, that is in crystals without inversion symmetry. Among the second order nonlinear processes, which can be described as three-wave interactions the simplest is the second harmonic generation (SHG) for which, under proper conditions, the power in the incident beam at ω is converted to frequency 2ω . If the optical field that impinges on the nonlinear medium consists of two distinct frequency components ω_1 and ω_2 , it is possible to obtain a component of the field at $\omega_3 = \omega_1 + \omega_2$. This interaction is called sum frequency generation (SFG). Note that the SHG can be seen as a degenerate case of the SFG, which occurs when $\omega_1 = \omega_2$. A third kind of interaction occurs when the generated wave has a frequency $\omega_3 = \omega_1 - \omega_2$, which is known as difference frequency generation (DFG). A schematic image of this three main second-order nonlinear processes is shown in figure (1.1).

In nonlinear optics it is often used a compact notation for the $\chi^{(2)}$ rank-three tensor, exploiting its symmetries. Let us introduce the tensor $\underline{\underline{d}}$, for which

$$d_{ijk} = \frac{1}{2} \chi_{ijk}^{(2)} \quad (1.2)$$

Under Kleinman symmetry conditions the tensor $\underline{\underline{d}}$ is symmetric in the last two indices, and it is therefore possible to introduce the Voigt contracted notation:

$$\left| \begin{array}{l} jk : \\ l : \end{array} \begin{array}{cccccc} 11 & 22 & 33 & 23, 32 & 31, 13 & 12, 21 \\ 1 & 2 & 3 & 4 & 5 & 6 \end{array} \right| \quad (1.3)$$

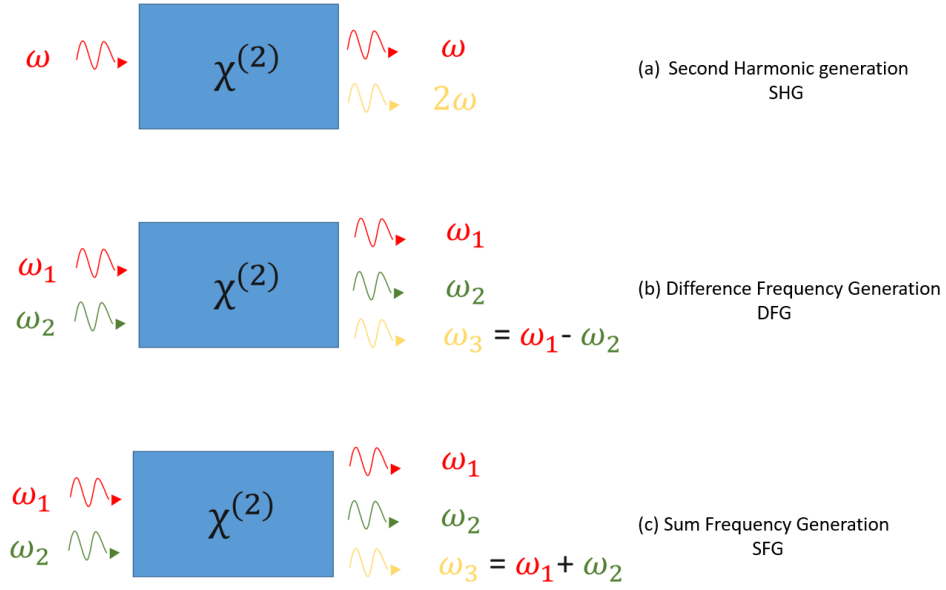


Figure 1.1: Different $\chi^{(2)}$ nonlinear processes

which simplifies the nonlinear tensor into a 3x6 matrix:

$$\underline{\underline{d}} = \begin{pmatrix} d_{11} & d_{12} & d_{13} & d_{14} & d_{15} & d_{16} \\ d_{21} & d_{22} & d_{23} & d_{24} & d_{25} & d_{26} \\ d_{31} & d_{32} & d_{33} & d_{34} & d_{35} & d_{36} \end{pmatrix} \quad (1.4)$$

The particular form of such tensor is specific for each crystalline class.

It is crucial to define the physical conditions under which the second-order nonlinear effects can occur. In order to understand this, it is necessary to solve the wave equation in a non linear medium:

$$\nabla^2 E - \frac{n^2}{c^2} \frac{d^2 E}{dt^2} = \frac{1}{\epsilon_0 c^2} \frac{d^2 P^{NL}}{dt^2} \quad (1.5)$$

where P^{NL} is the non linear term of the polarization vector P . Starting from this equation, it is possible to show that the amplitude A_3 of the slowly varying envelope of the field at ω_3 satisfies the equation:

$$\frac{dA_3}{dz} = \frac{2id_{\text{eff}}\omega_3^2}{k_3 c^2} A_1 A_2 e^{i\Delta k z} \quad (1.6)$$

where A_1 and A_2 are the envelope amplitudes at ω_1 and ω_2 , respectively and d_{eff} is the effective value of the tensor $\underline{\underline{d}}$. The factor $\Delta k = k_1 + k_2 - k_3$ is called the momentum mismatch and plays a crucial role in the amplitude of the field A_3 . If we consider the special case of $\Delta k = 0$, called

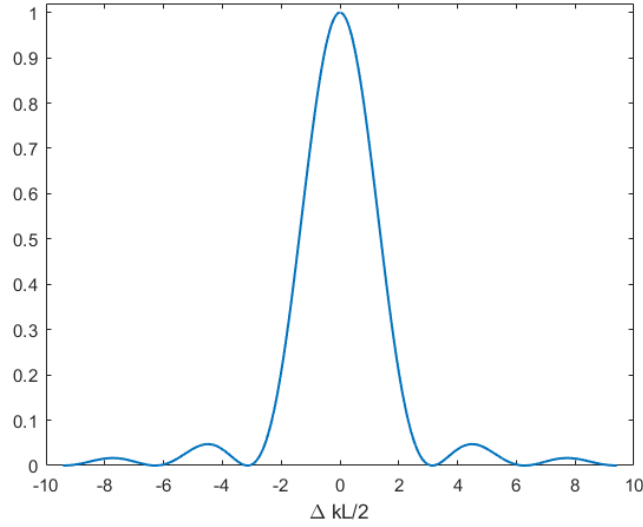


Figure 1.2: Effects of wavevector mismatch on the efficiency of sum-frequency generation

phase matching condition, A_3 increases linearly with the spatial position z . Conversely if the phase matching condition is not fulfilled the intensity A_3 is smaller than for the case of $\Delta k = 0$. Integrating equation (1.6) over a distance L , can be readily found that

$$|A_3|^2 \propto L^2 \text{sinc}^2\left(\frac{\Delta k L}{2}\right) \quad (1.7)$$

This expression predicts a rapid decrease of the efficiency of the sum frequency generation for $\Delta k \neq 0$. Achieving the phase matching condition is in general not trivial because the refractive index of materials is an increasing function of the frequency (normal dispersion). In bulk media is possible to exploit the natural birefringence of the crystal to achieve phase matching; otherwise it is possible to create a periodic structure to achieve the so called quasi-phase matching.

Depending on the polarization of the waves involved, there are two types of phase matching. Type I phase matching is the case in which the low-frequency waves (ω_1 and ω_2) have the same polarization and type II is the case where the polarizations are orthogonal.

1.1 Propagation of the electromagnetic field into a waveguide

Optical waves can be confined in a transnational invariant dielectric structure with a small cross sectional and a refractive index higher than that of the surrounding medium. In such waveguides, light can be guided through successive total internal reflections at the boundaries. A waveguide media of nonlinear optical materials allows strong nonlinear interaction over a long interaction length. In waveguide structures one can exploit the different values of the effective indices of the modes to achieve mode-dispersion phase matching.

Taking the z axis as the propagation axis, the distribution of the refractive index can be written

as $n(x, y)$ and the electric field of the wave as:

$$E(x, y, z) = E(x, y)e^{-i\beta z} \quad (1.8)$$

where β is the propagation constant. The field has a transverse profile $E(x, y)$ and a propagation term $e^{-i\beta z}$ along z . Substituting this expression of the field into the Helmholtz equation:

$$\left[\frac{d^2}{dx^2} + \frac{d^2}{dy^2} + \left(\frac{\omega^2}{c^2} n^2(x, y) - \beta^2 \right) \right] E(x, y) = 0 \quad (1.9)$$

This equation has a discrete number of solutions that are the modes of the waveguide. If β is real the mode is a guided mode and it is possible to define an effective index for that mode $n_{\text{eff}} = \beta \cdot c / \omega$. Guided modes with $E_y = 0$ and whose main field component is $E_x(x, y)$ are called TE-like mode; there also exists guided modes with $E_x = 0$ and dominant component $E_y(x, y)$ that are designated as TM-like modes.

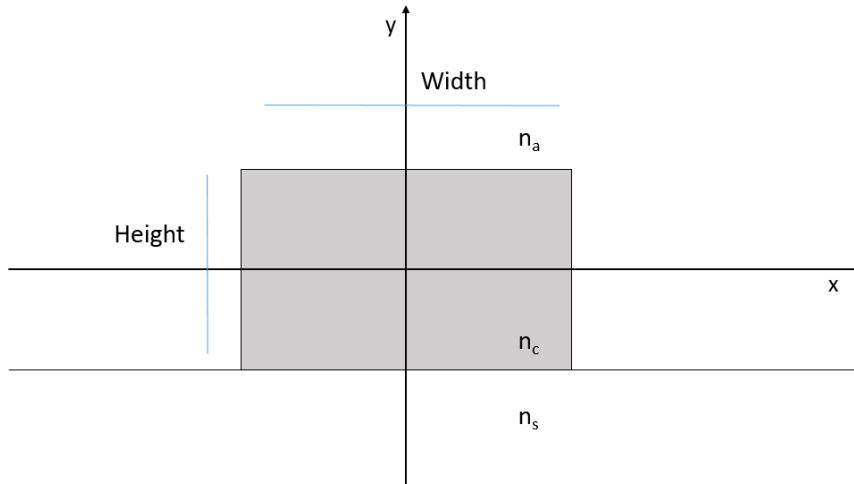


Figure 1.3: Schematic cross section of a rectangular channel waveguide. The labels n_a, n_c and n_s refer to the refractive indices of air, core and substrate respectively

Chapter 2

Design of the device

The device that we aim to design is a chip-scale nonlinear waveguide for efficient sum frequency generation (SFG). Such waveguide will be excited with two waves at ω_1 and ω_2 and, thanks to the second-order non linear interaction, it will generate a wave at $\omega_3 = \omega_1 + \omega_2$. Such a device is supposed to convert a mid-infrared wave to a wave that falls in the near infrared spectrum (around $\lambda = 1000$ nm), via three-wave mixing with of a pump wave. Since the mid-infrared wave can fall in a relative wide spectrum (approximately from $\lambda = 2500$ nm to $\lambda = 4000$ nm), it is necessary that the device is tunable over a broad spectral range. The material used to realize the guides is $\text{Al}_x\text{Ga}_{1-x}\text{As}$ with a given molar fraction x of Aluminum (Al) added. The band gap of the material can be engineered by changing the Al concentration x . The $\text{Al}_x\text{Ga}_{1-x}\text{As}$ is a non-centrosymmetric crystal with a strong quadratic non linearity. Its nonlinear tensor $\underline{\underline{d}}$ has the form:

$$\underline{\underline{d}} = \begin{pmatrix} 0 & 0 & 0 & d_{14} & 0 & 0 \\ 0 & 0 & 0 & 0 & d_{14} & 0 \\ 0 & 0 & 0 & 0 & 0 & d_{14} \end{pmatrix} \quad (2.1)$$

where $d_{14} = 119$ pm/V at $\lambda = 1500$ nm. This tensor structure makes it necessary that both x y components of the electric field are non-zero otherwise the nonlinear interaction vanishes. Our waveguide is therefore required that the waveguide to be along the [110] directions of the (Al)GaAs.

Once we have phase matching, high SFG efficiency requires to maximise the waveguide length, because the intensity of the signal at ω_3 is proportional to the square of the distance traveled in the guide. On the other hand, the upper limit for the waveguide length is the loss of the guide. Therefore it is crucial to minimize losses to have long waveguide. In general, as order of magnitude, losses <0.5 cm⁻¹ can be achieved, and this sets a maximum length for the guide of more than 2 cm. Further details will be given about the materials and structures used to obtain a low-loss waveguide.

Another important feature to consider is the overall geometry of the guide. The idea of the device is that it should be compact and integrable on-chip: in other words, it must occupy the smallest area possible. Of course there are many possible valid geometries. One very compact geometry is a spiral-shape, but the physical considerations in terms of phase-matching and tunability of such a shape would be quite complicated.

The solution adopted is a slalom shape: a straight waveguide of length 1 mm is followed by a

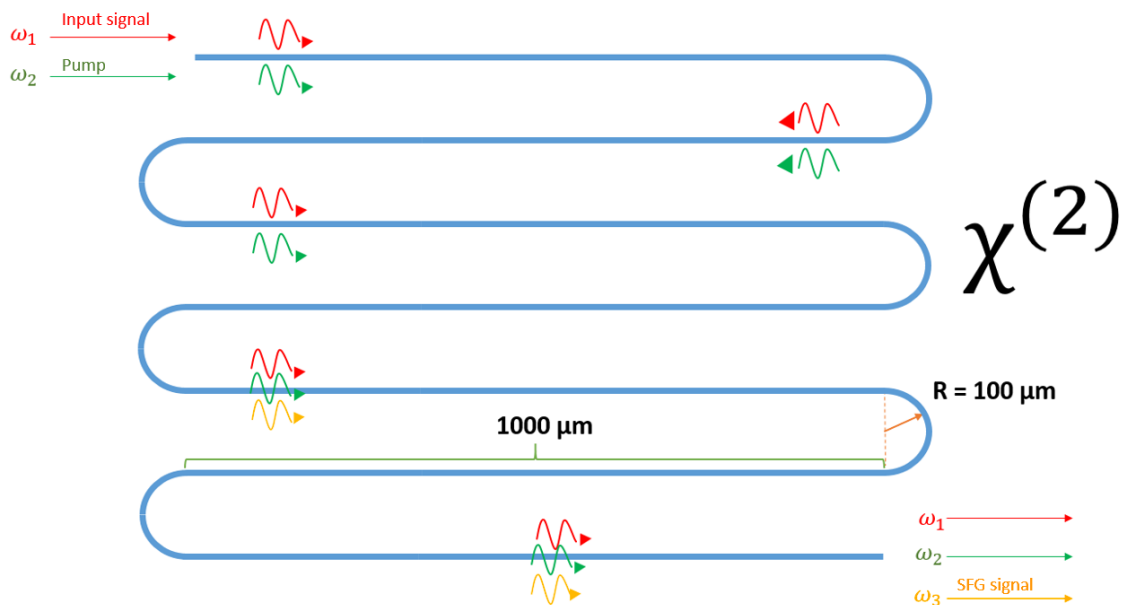


Figure 2.1: Geometry of the waveguide

half-arc guide with radius $100 \mu\text{m}$. This geometry allows to store in 1 mm^2 a guide with a length of roughly 0.75 cm . The schematic of the geometry is depicted in figure (2.1). In the following two different kind of structures and materials for the waveguides will be analyzed:

- 1) a low index contrast waveguide with an $\text{Al}_{0.22}\text{Ga}_{0.78}\text{As}$ on top of $\text{Al}_{0.8}\text{Ga}_{0.2}\text{As}$ cladding.
- 2) a high index contrast waveguide made in $\text{Al}_{0.18}\text{Ga}_{0.82}\text{As}$ on top of SiO_2 .

2.1 Low-contrast waveguides

2.1.1 Design of the straight waveguide

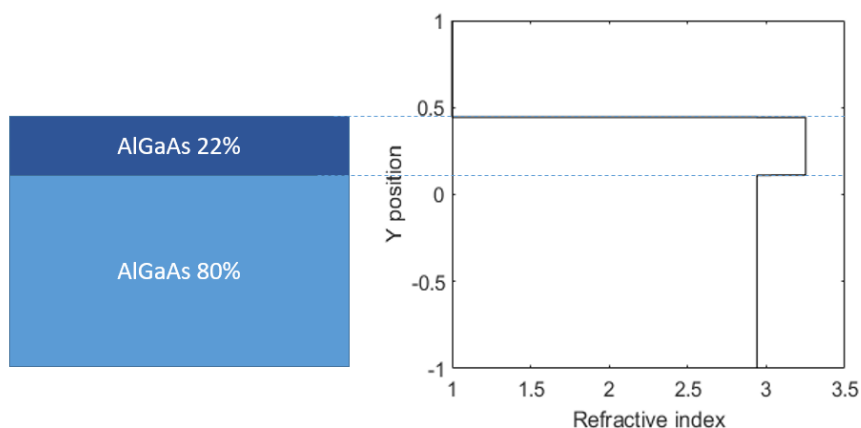


Figure 2.2: Index Profile

Structure 1) is a low-contrast: the material for the core is AlGaAs with 22% of aluminum and the cladding below is made again of AlGaAs with an higher concentration of aluminum (80%).

The increment of Al in the material has two consequences: increasing the band gap of the material and the lowering of the refractive index of the same. The theoretical value of the refractive index ($\lambda = 1550$ nm) of the $\text{Al}_{0.22}\text{Ga}_{0.78}\text{As}$ is $n = 3.25$ compared to the refractive index of $\text{Al}_{0.8}\text{Ga}_{0.2}\text{As}$ which is $n = 2.96$. The theoretical band gap of the $\text{Al}_{0.22}\text{Ga}_{0.78}\text{As}$ is $E_g = 1.696$ eV which corresponds to $\lambda = 731$ nm. It is useful to consider the energy band gap of the core because for high energy (i.e. small λ) of the incident waves two photon absorption may occur; this phenomenon can be detrimental for the performances of the device.

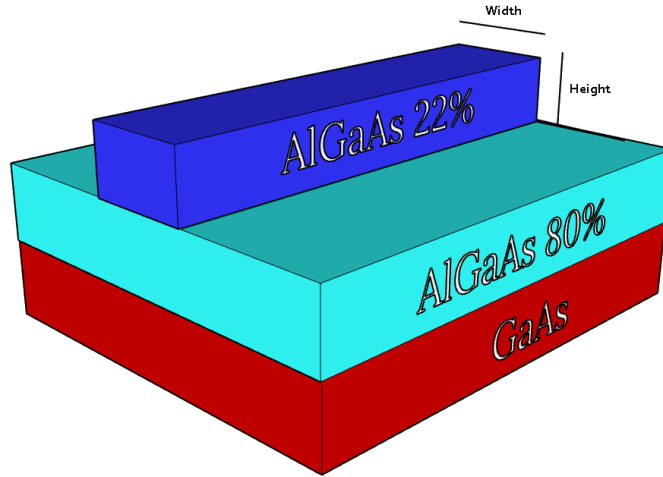


Figure 2.3: Sketch of the structure for the low contrast index waveguides. The core is made of $\text{Al}_{0.22}\text{Ga}_{0.78}\text{As}$ and the cladding $\text{Al}_{0.8}\text{Ga}_{0.2}\text{As}$

The low contrast between core and cladding refractive indices results in poorly confined modes: this makes necessary to increase both core width and height in order to properly accommodate the modes in the waveguide and avoid that the field leaks to the high-index GaAs wafer. Because of such relatively large core, the modes sit in the center of the core and sees less the border of the core itself. The lateral wall sides of the waveguides usually have some imperfections due to fabrication issues and consequently the fact that the field stays relatively far apart from the border avoid important scattering phenomena during the transmission and this lower the losses of the waveguide. Let us stress again the importance for this kind of devices of keeping the losses as low as possible, in order to allow long waveguide and thus increasing the overall efficiency of the nonlinear interaction. This constitutes the main advantage of structure number 1).

The first step to determine waveguide width and height is to choose the degeneracy point, which means to choose three wavelength λ_1, λ_2 and λ_3 such that $\lambda_1 = \lambda_2 = \frac{\lambda_3}{2}$. The degeneracy point sets the upper limit for λ_3 , which is the SFG wavelength, so it is necessary to choose properly this wavelength. Our choice here is to set $\lambda_3 = 1040$ nm and consequently $\lambda_1 = \lambda_2 = 2080$ nm. Then it is required to find the proper geometry that guarantees the phase matching condition $\beta_1 + \beta_2 = \beta_3$ for the three selected wavelengths. The phase-matching condition can be rewritten as:

$$\frac{2\pi}{\lambda_1} n_1^{eff}(\lambda_1) + \frac{2\pi}{\lambda_2} n_2^{eff}(\lambda_2) = \frac{2\pi}{\lambda_3} n_3^{eff}(\lambda_3) \quad (2.2)$$

which at degeneracy can be rewritten simply as:

$$n_1^{eff}(\lambda_1) + n_2^{eff}(\lambda_2) = 2n_3^{eff}(\lambda_3) \quad (2.3)$$

In order to fulfill equation (2.2) one has to consider three different modes, one for each wavelength; each mode is characterized by its effective index n_{eff} , which depends on a few factors: the materials, the geometry of the waveguide, the wavelength, the mode polarization (TE, TM). As recalled in the theoretical introduction, the use of waveguides allows phase matching by mode-dispersion. The mode index depends upon the waveguide dimension and the mode order and takes a value between the refractive indices of the core and the cladding for each wavelength. Thus in principle it is possible to select the proper geometry and the modes that allow the phase matching at the selected wavelengths.

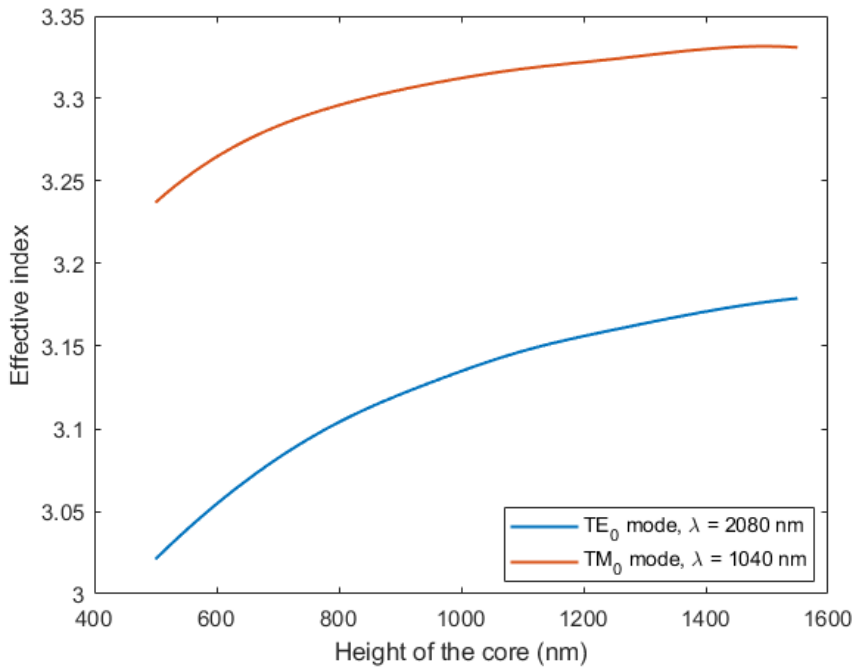


Figure 2.4: Effective indices of the fundamental TE and TM mode as function of the height of the core. It is not possible to reach the phase matching condition for any value of the height

There are two types of phase matching, depending on the polarization of the modes involved. For type I phase matching, the input modes have the same polarization (e.g. TE) while the SHG signal has a different polarization (e.g. TM). On the contrary, in type II phase matching the input polarizations are orthogonal and therefore one will be TE while the other TM.

In general a type I phase matching is more convenient because it allows to work just with fundamental TE and TM modes, which are easier to excite with respect to higher order modes. However, as suggested by figure (2.4), it is not possible to find a geometry (width and height) that satisfies type I phase matching condition and therefore it is necessary to look for phase matching with higher-order modes. The picture shows the variation of the refractive indices of the modes as function of the height of the core for planar waveguides (i.e. infinite width). Since there is no intersection between the two curves over a wide range of heights, it is not possible

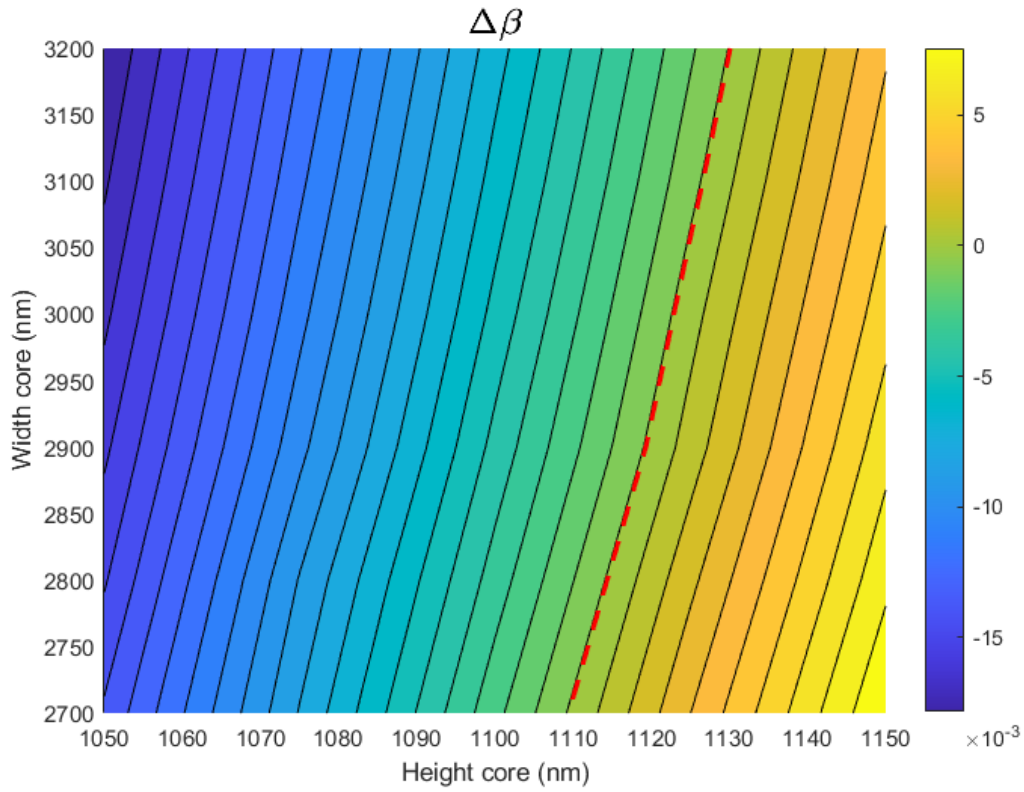
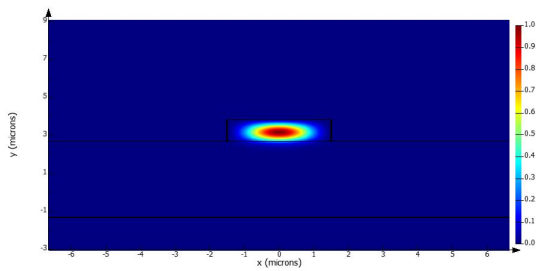
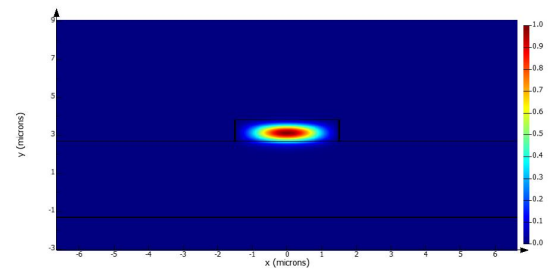


Figure 2.5: Map of the $\Delta\beta$ as function of the width and the height of the core. The modes considered are TM_{00} for the pump, TE_{00} for the input signal and TE_{20} for the output signal. The red dashed line represents the points where $\Delta\beta = 0$, i.e. the geometries for which the phase matching is reached.

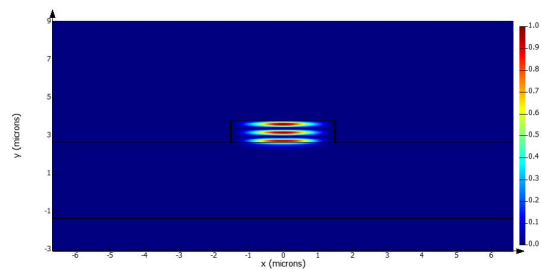
to find a geometry that fulfill type I phase matching.



(a) TE_{00} mode at 2080 nm



(b) TM_{00} mode at 2080 nm



(c) TE_{20} mode at 1040 nm

Figure 2.6: Electric field distributions for the three interacting modes

To find the proper geometry that fulfills type II phase matching, I performed a sweep both on the

height and the width of the core of the guide and numerically finding the effective indices of the three modes and then verifying if equation (2.2) is satisfied or not. All the numerical calculation are performed by means of the Finite-Difference Eigenmode (FDE) solver of Lumerical. This eigensolver find the modes by solving Maxwell's equations on a cross-sectional mesh of the waveguide by means of a finite-difference algorithm. Maxwell's equations are formulated into a matrix eigenvalue problem, which depends on the geometry and on the mesh, and are solved using sparse matrix techniques.

Since it is not possible to find a geometry allowing for phase matching among fundamental modes, I had to consider higher order modes: in particular a fundamental TE_{00} mode for the input signal, a fundamental TM_{00} mode for the pump and a TE_{20} mode for the SHG output. The values of the effective indices at degeneracy are $n_{\text{eff}} = 3.125$ (TE_{20}), $n_{\text{eff}} = 3.131$ (TE_{00}) and $n_{\text{eff}} = 3.118$ (TM_{00}).

Figure (2.5) shows the momentum mismatch $\Delta\beta$ of the effective indices of this modes as function of the different dimensions of the core. In particular, for a width of 3000 nm and a height of 1125 nm, I found the type II phase matching at $\lambda = 2080$ nm for both input signal and pump. and $\lambda = 1040$ nm for the SHG output. Figure (2.6) shows the distribution of the electric field for the three different modes. Since the waveguide will be used to perform SFG over a range of different wavelengths, I needed to evaluate the whole tunability curve of for this structure. Such curve represents all the λ_1 , λ_2 and λ_3 that satisfy both energy conservation law

$$\frac{2\pi c}{\lambda_1} + \frac{2\pi c}{\lambda_2} = \frac{2\pi c}{\lambda_3} \quad (2.4)$$

and the conservation of momentum

$$\frac{2\pi}{\lambda_1} n_1^{\text{eff}}(\lambda_1) + \frac{2\pi}{\lambda_2} n_2^{\text{eff}}(\lambda_2) = \frac{2\pi}{\lambda_3} n_3^{\text{eff}}(\lambda_3) \quad (2.5)$$

In order to obtain this curve I first evaluated the dispersion relation $n_1^{\text{eff}}(\lambda_1)$, $n_2^{\text{eff}}(\lambda_2)$ and $n_3^{\text{eff}}(\lambda_3)$ by means of the FDE solver of Lumerical.

Once the dispersion relation has been evaluated, I can find the three wavelengths that satisfy both (2.4) and (2.5). Figure (2.7) illustrates the tunability curve: the x-axis represent the wavelength of the output signal, while the y axis represent both the wavelength of the input signal (blue curve) and the pump (red curve). The intersection point is the degeneracy which occurs at 1040 nm for the output signal and 2080 nm for the input signal and the pump as predicted. The picture shows also the limit under which two photon absorption (TPA) occurs for AlGaAs with 22% of Al. Note that TPA can lower the effect of the desired nonlinear effect, in particular if we work with input pulsed laser. Adding a certain percentage of Al to GaAs was indeed made to lower the TPA threshold. However, this choice makes the refractive-index contrast between core and cladding weaker, resulting in less confined modes. It is therefore necessary to find the right compromise for the quantity of Al to add.

An important parameter to evaluate is the nonlinear conversion efficiency η_0 : indeed the phase matching condition is not sufficient to guarantee the SFG. This is due to the fact that the interacting modes must have a sufficient non-linear spatial overlap in order to have an efficient frequency up conversion.

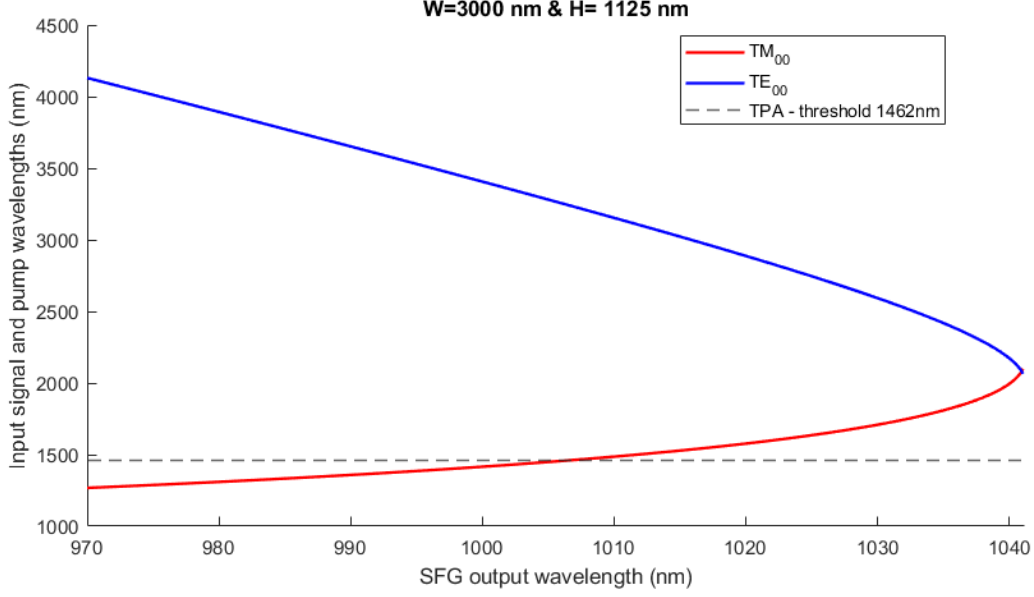


Figure 2.7: Tunability curve. The horizontal axis represents the wavelength of the SFG signal, TE_{20} mode. The vertical axis represents the wavelength of both the input signal (blue curve, TE_{00}) and the pump (red curve, TM_{00}) which are fundamental TE mode and fundamental TM mode respectively. The horizontal dashed line represents the limit below which two photon absorption (TPA) occurs for AlGaAs with 22% of Al

$$\eta_0 = \frac{8\pi^2}{\epsilon_0 c \lambda_1 \lambda_2} \frac{d_{14}^2}{n_{\text{eff}}(\lambda_1) n_{\text{eff}}(\lambda_2) n_{\text{eff}}(\lambda_3)} \left[\iint d(x, y) E_{TE_{00}}(\lambda_1) E_{TM_{00}}(\lambda_2) E_{TE_{20}}(\lambda_3) dx dy \right]^2 \quad (2.6)$$

where $E_{TE_{00}}(\lambda_1)$, $E_{TM_{00}}(\lambda_2)$ and $E_{TE_{20}}(\lambda_3)$ are the normalized electric field of the three different modes; $n_{\text{eff}}^{\lambda_1}$, $n_{\text{eff}}^{\lambda_2}$ and $n_{\text{eff}}^{\lambda_3}$ are the effective indices. Moreover $d(x, y)$ is the cross-sectional distribution of nonlinear optical coefficient normalized to d_{14} .

The modal overlap depends both on the susceptibility tensor $\chi^{(2)}$ and on the spatial geometrical overlap between the components of the electric field of the different modes. This implies that there are sort of selection rules on the symmetries of the modes involved in the interaction. In particular it is necessary that the overall integrated function is even: the modes involved must therefore exhibit the same symmetry. Moreover the interaction must occur along a proper crystallographic direction that guarantees that the $\chi^{(2)}$ tensor does not vanish. The conversion efficiency has been evaluated for different wavelengths: at degeneracy ($\lambda_1 = \lambda_2 = 2080$ nm and $\lambda_3 = 1040$ nm) $\eta_0 = 10.02 \text{ W}^{-1} \text{ cm}^{-1}$. Moving away from degeneracy, and thus lowering λ_3 the non-linear efficiency parameter has the tendency to decrease. In particular at $\lambda_3 = 1015$ nm a value of $\eta_0 = 8.31 \text{ W}^{-1} \text{ cm}^{-1}$ is found and $\eta_0 = 7.03 \text{ W}^{-1} \text{ cm}^{-1}$ at $\lambda_3 = 1000$ nm .

2.1.2 Design of the arc-shape waveguide

So far, only the straight part of the waveguides has been considered for the design. Further considerations are needed to take into account the arc-shaped waveguides, because there is a shift in the effective indices of the modes in the arched part, and moreover the value of the $\chi^{(2)}$ tensor changes along the curve.

First of all, for a half circle of radius R , the wave propagating along the curve will accumulate a phase shift given by $\Delta\beta_{arc} \cdot \pi R = m\pi$, where $\Delta\beta_{arc} = \beta_{arc}^{\lambda_1} + \beta_{arc}^{\lambda_2} - \beta_{arc}^{\lambda_3}$ is the difference of the three wavenumbers of the modes inside the arc. The modes inside the curved waveguides have a different shape and different values of the effective indices. It is crucial to notice that the difference between such effective indices has important consequences on the phase-matching condition: indeed in general it is not guaranteed that a triplet of modes that are phase matched along the straight waveguide are still phase matched along the curve. This is of course an important issue that must be tackled in the design of the device.

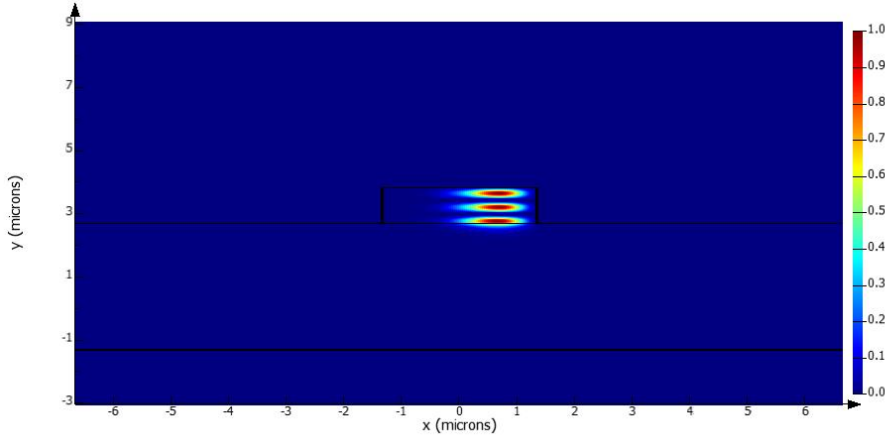


Figure 2.8: Image of the TE_{20} mode at $\lambda = 1040$ nm in a curved waveguide with radius $100 \mu\text{m}$. The lobes of the mode are shifted towards the external side of the curvature

Figure (2.8) shows the TE_{20} mode at $\lambda = 1040$ nm: the mode is shifted inside the core towards the external side of the curvature. Furthermore, when moving along the curve, the tensor product between $\chi^{(2)}$ and the three fields will not take a constant value, since the fields explore different directions within the crystal; due to the symmetry of the $\bar{4}$ crystal, the normalized tensor will assume a value $\underline{\underline{d}}(l) = \cos(2l/R)$ along the curvature where l is a position parameter along the waveguide. The amplitude $A(l)$ of the SHG mode is described by:

$$\frac{dA(l)}{dl} = i\underline{\underline{d}}(l)e^{-i\Delta\beta(l)l} \quad (2.7)$$

where $\underline{\underline{d}}(l) = 1$ along the straight waveguides. In order to properly understand the behaviour of the three different modes under this condition let us start from the degeneracy ($\lambda_1 = \lambda_2 = 2080$ nm; $\lambda_3 = 1040$ nm). In this case, since the waveguide is properly designed, $\Delta\beta = 0$ along the straight path, the value of $\underline{\underline{d}}(l)$ is constant, and thus the solution of equation (2.7) is simply $A(l) = il$, so that the amplitude increases linearly along the imaginary axis in the complex plane. Obviously its square modulus $|A|^2 = l^2$ according to the usual quadratic relation between the amplitude of the second harmonic and the length l of the waveguide. On the other hand, the behavior of the amplitude A along the curve depends on the particular value of $\Delta\beta_{arc} \cdot \pi R = m\pi$.

Let us now focus on the behavior of the second harmonic for different integer values of m . For odd values of m , the wave generated in the second straight waveguide destructively interferes with the wave generated in the first straight waveguide, with the net result that the overall

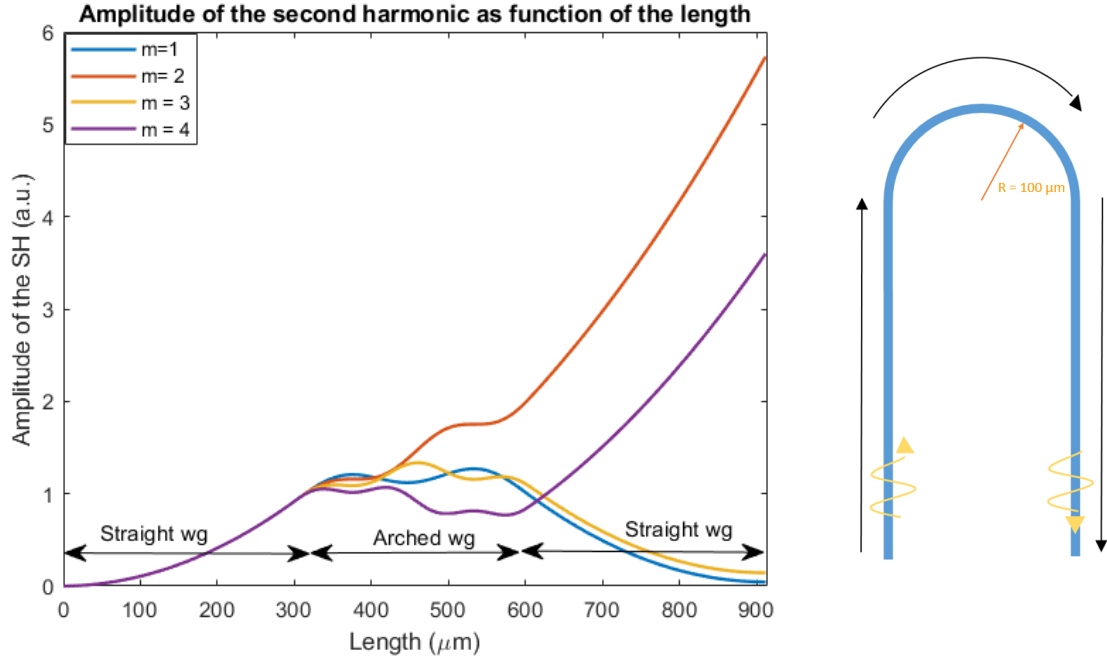


Figure 2.9: $|A|^2$ of the second harmonic in a U-shaped waveguide, for different values of m . The two straight parts have a length of $300 \mu\text{m}$ each and the radius is $100 \mu\text{m}$. For odd values of m , there is destructive interference at the exit of the curve and the amplitude drop (yellow and blue lines). For even values of m , the amplitude of the second harmonic further increases after the curve (purple line). For the special case $m = 2$ (red line), there is a quasi-phase matching, thus the second harmonic partially increases in amplitude even along the arc.

amplitude along the structure does not increase. On the contrary, for even values of m there is a constructively interference between the waves in the two straight parts of the waveguide and the overall result is an increasing the second harmonic amplitude. Note, however, that along the curvature there is no net gain in the amplitude. For the particular case of $m = 2$, the wavevector mismatch is compensated by the modulation of the nonlinear optical coefficient by $\cos(2l/R)$, and thus a quasi-phase matching condition is reached. The phase difference condition, $\Delta\beta_{arc} \cdot \pi R = 2\pi$ is equivalent to the 4-QPM condition.

Figure (2.9) shows the square modulus of the amplitude of the second harmonic as function of the length traveled by the wave in the U-shaped waveguide with two $300 \mu\text{m}$ straight parts and half circle with radius $R = 100 \mu\text{m}$. In the first straight part, the SHG amplitude increase quadratically with the length because of phase matching. Along the arc, it oscillates keeping a more or less constant value (save the case $m = 2$) and finally the behavior in the last straight part depends on the value of m .

In order to gain a better insight on how the SHG amplitude A evolves along the guide, it is possible to show in the complex plane the real and imaginary part of A . Fig(2.10) shows the phasor A in the complex plane when the wave propagates along the curve. For $m = 1$ and $m = 3$ (odd values) the phasor describes a half hypocycloid and a half epicycloid respectively and thus the phasor turn in the negative direction along the imaginary axis. For $m = 4$, the curve described by the amplitude is a full epicycloid, that the end of the entire arc the direction on the imaginary axis is positive. Lastly, for $m = 2$, the curve described by the phasor is a cycloid-curve that increases in amplitude during the propagation.

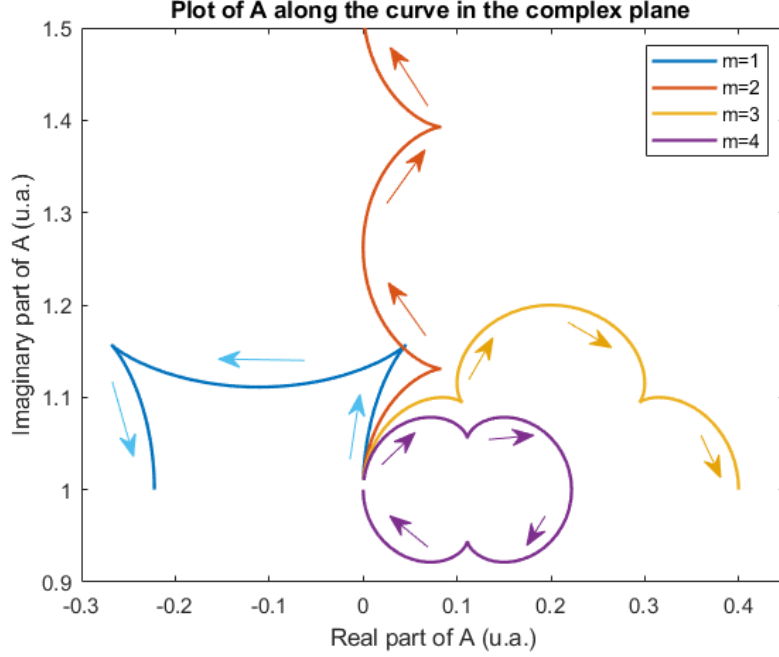


Figure 2.10: Phasor of the SHG amplitude A along a half circle in the complex plane, for different values of m . For $m = 1$ and $m = 3$ the curves described are half cycloids and thus end in the negative direction, whereas for $m = 4$ the curve is a full cycloid that ends in the positive direction. For the particular case $m = 2$ the cycloid is not a closed line and the amplitude of the phasor increases along the arc.

In conclusion, $m = 2$ is the best condition to achieve because it guarantees a partial gain in the curvature and a constructive interference between the waves. It should be possible in principle to design the curved part of the guide such that this condition is obtained at degeneracy. This means to find the proper width of the curved wave guide such that the condition $\Delta\beta_{arc} \cdot R = 2$ is satisfied at degeneracy (the procedure to find the proper geometry would be very similar to the one used to obtain the phase matching condition in the straight waveguide). But unfortunately, even if the proper width is obtained, the QPM condition would be satisfied only for one particular point ($\lambda_1 = \lambda_2 = 2080$ nm and $\lambda_3 = 1040$ nm). Indeed if one consider different wavelengths on the tunability curve (that are the points where $\Delta\beta = 0$ only on the straight guide), it is not longer guaranteed that the QPM $m = 2$ condition is still valid on the arc. Of course this is a problem that undermine the proper tunability and functionality of the entire device.

2.1.3 Tunability of the entire structure

In order to understand the behavior of the structure, it is necessary to study the entire device under different input wavelengths λ_1 and λ_2 , and then evaluate the amplitude $|A|_{\omega_3}$ of the mode at λ_3 . To this end, let us consider a unit cell of the structure which is composed by a straight waveguide of length $500 \mu\text{m}$, followed by an arc waveguide with $R = 100 \mu\text{m}$, again followed by a straight waveguide with length $1000 \mu\text{m}$, followed by a second arc of the same radius and finally the last straight part long as the first. The total length of the unit cell is 2.683 mm. The schematic of the unit cell is illustrated in fig (2.11). The entire device will be a repetition of this unit cell. Let two waves impinge at λ_1 and λ_2 (i.e. ω_1 and ω_2), with a relative phase difference $\Delta\phi$ that is set to zero for convenience. The phase difference at the end of the cell depends on the distance traveled and the $\Delta\beta$ of the waves along the different segments of the cell. The final

phase $\Delta\phi_f$ at the end of the cell is given by:

$$\Delta\phi_f = \Delta\beta l_1 + \Delta\beta_{arc} l_2 + \Delta\beta l_3 + \Delta\beta_{arch} l_4 + \Delta\beta l_5 \quad (2.8)$$

where $\Delta\beta$ and $\Delta\beta_{arc}$ are the momentum mismatches for the straight and curved part respectively, l_1, l_3, l_5 are the lengths of the three straight parts, and l_2, l_4 the lengths of the arc-shaped parts.

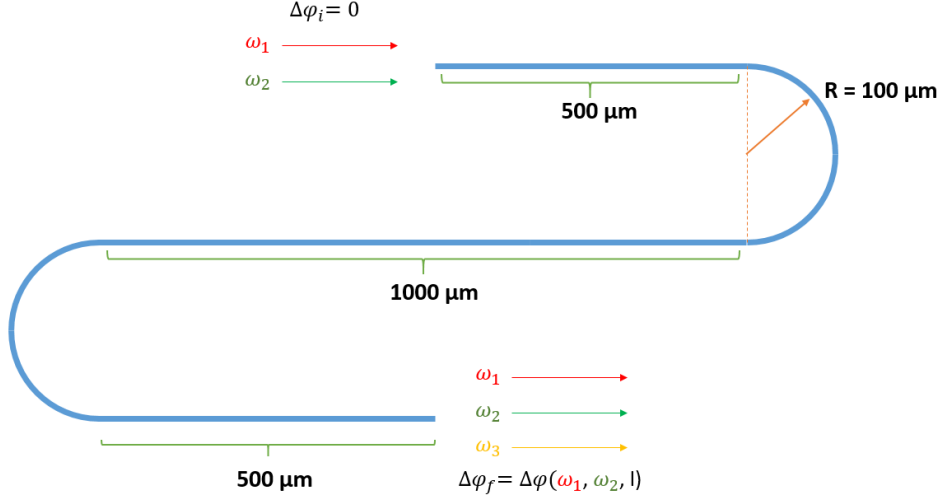


Figure 2.11: Schematic of the unit cell of the structure. Two waves ω_1 and ω_2 impinge at the entrance with a relative difference of phase $\Delta\phi$ set to 0 for convenience. The difference of phase at the end of the cell, $\Delta\phi_f$, depends both on the distance traveled and the different $\Delta\beta$'s along the structure.

Note that the initial phase of the following cell is the final phase $\Delta\phi_f$ of the previous cell and the amplitude A_{ω_3} at the exit of each cell is strongly influenced by the value of the initial phase. Indeed the difference of phase at the entrance of the cell affects the interference that can be constructive rather than destructive. In order to evaluate the value of A_{ω_3} after a cell for two impinging ω_1 and ω_2 it is necessary first to evaluate both $\Delta\beta$ and $\Delta\beta_{arc}$ for the triplet ω_1, ω_2 and $\omega_3 = \omega_1 + \omega_2$. Then perform the integral given by equation (2.6) over each segment of the unit cell:

$$A_{\omega_3} = i \cdot \left[\int_{l_1} e^{-i\Delta\beta l + \phi_0} dl + \int_{l_2} \cos(2l/R) e^{-i\Delta\beta_{arc} l + \phi_1} dl + \int_{l_3} e^{-i\Delta\beta l + \phi_2} dl + \int_{l_4} \cos(2l/R) e^{-i\Delta\beta_{arc} l + \phi_3} dl + \int_{l_5} e^{-i\Delta\beta l + \phi_4} dl \right] \quad (2.9)$$

where ϕ_1, ϕ_2, \dots are the cumulated phases along each segment of the cell and ϕ_0 is the initial phase. In order to evaluate the whole A_{ω_3} along the structure, it is necessary to calculate equation (2.9) as many times as necessary, considering a new ϕ_0 for each iteration. Of course A_{ω_3} must be evaluated on different values of ω_1 and ω_2 (or λ_1 and λ_2).

Figure (2.12) shows the square modulus of the amplitude $|A_{\omega_3}|^2$, in logarithmic scale and arbitrary units, as function of λ_1 and λ_2 , for five unit cells (i.e. a total length of 1.31 cm) of the waveguide. The colored area in the figure represent thus the points for which the couple λ_1 and λ_2 produce a significant non linear interaction (SFG) along the entire waveguide. In the right image, which is a zoomed image of the first, it is possible to better appreciate the fringes of $|A_{\omega_3}|^2$, which are reminiscent of the fringes of a typical $\text{sinc}^2(x)$ function. This image shows that the entire structure presents its own tunability. Figure(2.13) shows the fringes of interference

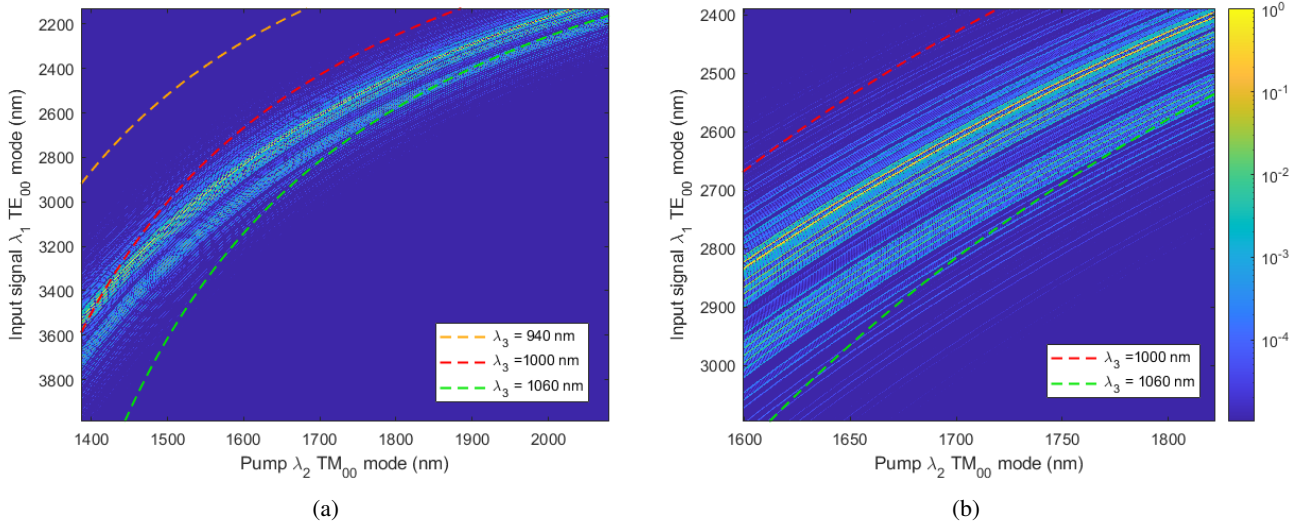


Figure 2.12: a) $|A_{\omega_3}|^2$ in logarithmic scale and arbitrary units as function of λ_1 and λ_2 , for a structure composed by 5 unit cells (total length of the guide is 1.31 cm). The colored area represents the region where the SFG intensity is high. The dashed lines represent the loci of constant λ_3 . (b) Zoomed image of the previous

evaluated for different λ_3 .

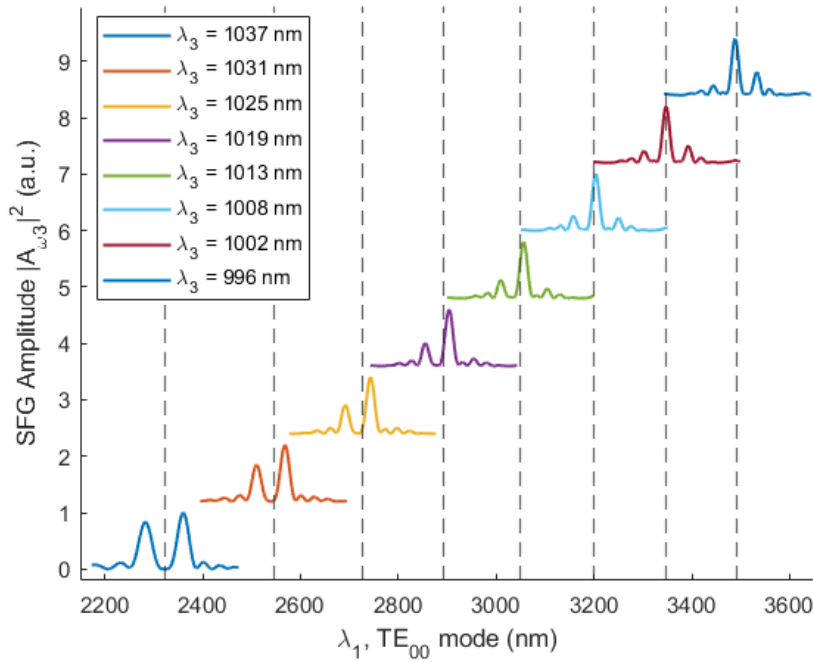


Figure 2.13: SFG amplitude $|A_{\omega_3}|^2$ as a function of λ_1 , for different fixed values of λ_3 . The vertical lines represent the points for which there would be a maximum in a straight waveguide with the same width and height of the core.

The figure shows the amplitude $|A_{\omega_3}|^2$ as function only of the wavelength of the TE₀₀ mode λ_1 for different fixed wavelength of the TE₂₀ mode λ_3 . Since changing one of the wavelength and fixing the other will change the value of the $\Delta\beta(\lambda_1, \lambda_2, \lambda_3)$, one would expect in this figure to find

the curves that characterize the relation between the amplitude and the momentum mismatch:

$$|A_3|^2 \propto L^2 \text{sinc}^2\left(\frac{\Delta\beta L}{2}\right) \quad (2.10)$$

However, in this more complex geometry, where straight waveguides are alternated by curved waveguides and the phase matching condition changes along the different types of guides, the shape of the square modulus of the SHG amplitude it is no longer $\propto \text{sinc}^2(x)$. It is interesting to note, the presence of a double peak in the amplitude, especially for low values of λ_1 . The higher the wavelength, however, the lower the second peak. The vertical dashed lines represent the position of the maximum of the peak of the $\text{sinc}^2(x)$ for a straight waveguide with the same width and height. It is worth noticing that in the slalom waveguides the peaks are slightly shifted due to the presence of the curved parts. Finally, the existence of a SHG peak of intensity for the square modulus of the amplitude of the TE_{20} mode at different λ_3 confirms that this kind of geometry waveguides presents its own tunability.

2.2 High-contrast waveguides

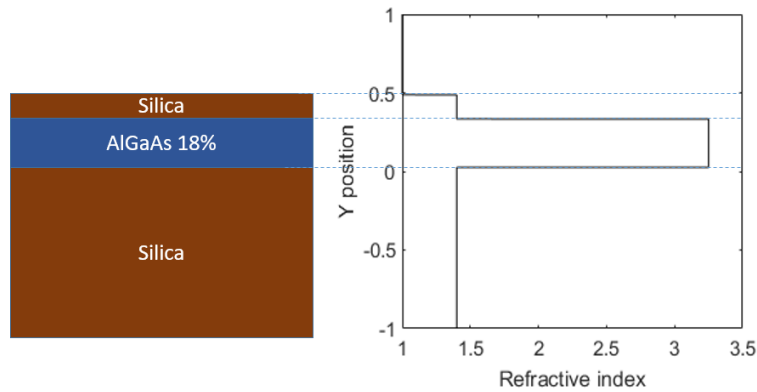


Figure 2.14: Index Profile

The second kind of waveguide that I have considered for fabrication is a high contrast. In this case the core material is AlGaAs with a slightly lower Al concentration (18%) which lays on a SiO_2 cladding and the whole structure sits on a Silicon wafer. The theoretical value of the refractive index of the $\text{Al}_{0.18}\text{Ga}_{0.82}\text{As}$ at $\lambda = 1550$ nm is about $n = 3.28$, while $n = 1.45$ for SiO_2 . Note that the fabrication of this kind of waveguides requires a wafer bonding process between the III-V semiconductor wafer and the SiO_2 on Silicon wafer; some further details will be provided in the following.

The schematic of the structure is depicted in figure (2.15). Furthermore a passivation layer in SiO_2 deposited by PECVD on top of the guide has been considered.

Since there is a high index contrast between the core and the cladding, it is not necessary in principle to consider relative large dimensions for the guide (with respect to the previous kind of structure). Now the modes in this case will be more tightly confined, and the good quality of the SiO_2 (especially if compared to the quality of the native oxide AlO_x) guarantees low loss even for this type of structure.

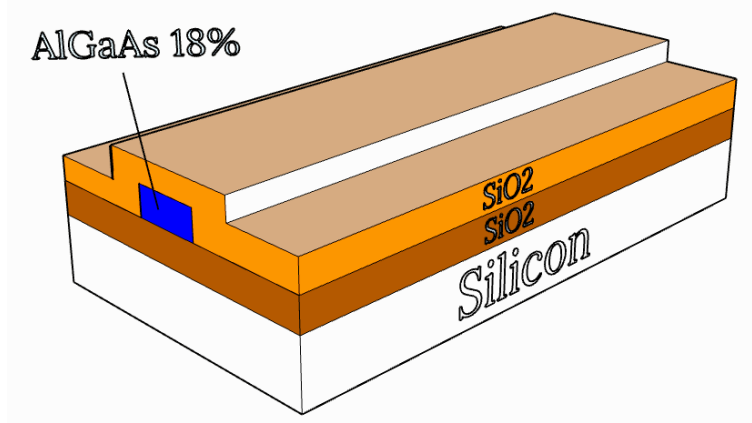


Figure 2.15: Schematic of the high-contrast waveguides

In order to find the core dimensions (width and height) that guarantee phase matching, I followed the same logical steps as in section 2.1. The degeneracy point in this case is chosen at $\lambda_1 = \lambda_2 = 2160$ nm and $\lambda_3 = 1080$ nm: this will shift the tunability curve towards higher values of λ for the input signal mode. In high-contrast structures it is possible to find type I phase matching: this means that $\Delta\beta = 0$ condition is reached for TE_{00} modes of the input signal and the pump and a fundamental TM_{00} mode for the output signal. Type I phase matching condition (2.4) at degeneracy ($\lambda_1 = \lambda_2$) can be rewritten in the form:

$$n_1^{\text{eff}}(\lambda_1) \equiv n_2^{\text{eff}}(\lambda_2) = n_3^{\text{eff}}(\lambda_3) \quad (2.11)$$

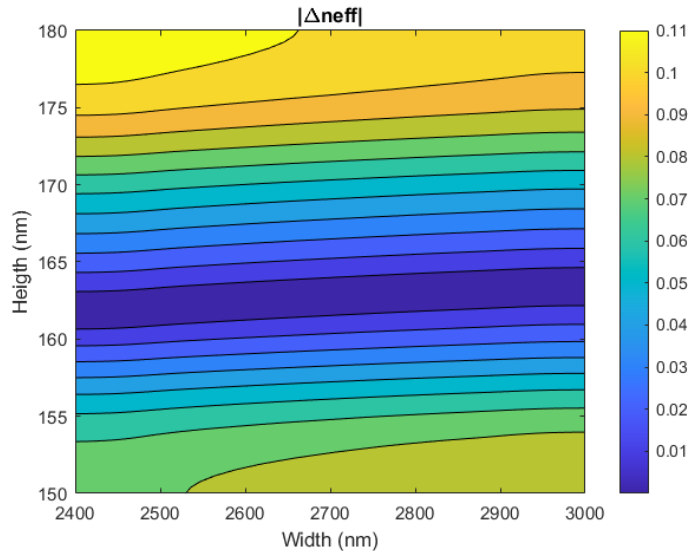


Figure 2.16: Absolute value of the difference between the effective indices of the TE_{00} evaluated at $\lambda_1 = 2160$ nm and the effective index of the TM_{00} mode evaluated at $\lambda_3 = 1080$ nm. The dark blue region represents the geometries for which the phase matching condition is reached.

It is then possible to evaluate $\Delta n^{\text{eff}} = n_1^{\text{eff}}(\lambda_1) - n_3^{\text{eff}}(\lambda_3)$ as a function of the width and the height of the waveguide core (for fixed λ_1 and λ_2). Figure (2.16) shows the difference in absolute

value between the TE_{00} mode at $\lambda_1 = 2160$ nm and TM_{00} mode at $\lambda_3 = 1080$ nm : the dark blue region corresponds to the geometries for which the phase matching condition is achieved. Note that the phase matching region is almost independent of the width. Since the device that we want to design should work at quite large λ_1 , it is convenient to choose a waveguide with a large width because it will better confine the long wavelength modes. Therefore a height of 163 nm and width of 3000 nm is chosen for this kind of waveguides. The electric-field distribution of both TM_{00} and TE_{00} modes at degeneracy ($\lambda_1 = \lambda_2 = 2160$ nm and $\lambda_3 = 1080$ nm) is plotted in figure (2.17). The effective index of the modes is $n_{\text{eff}} = 2.13$ for both modes.

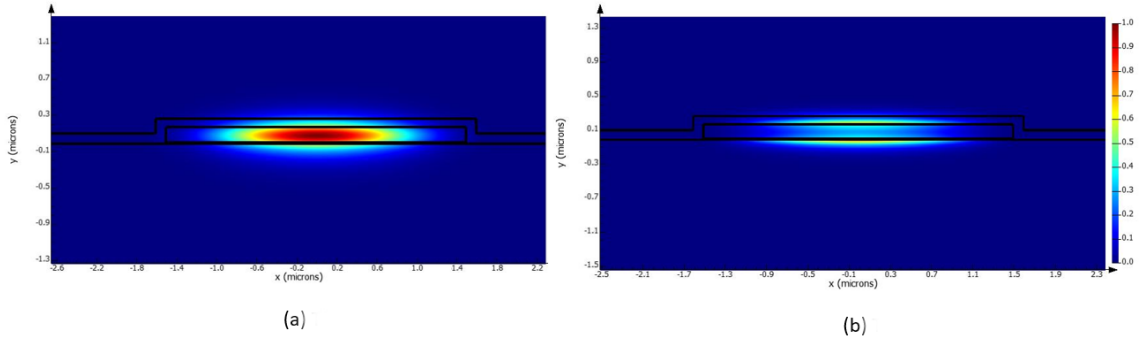


Figure 2.17: Distribution of the electric field for the TE_{00} mode at $\lambda = 2160$ nm (a) and the TM_{00} mode at $\lambda = 1080$ nm (b)

Once the width and height of the core are found, it is possible to evaluate the tunability for the straight guide. Similarly to the first kind of structure, it is necessary to consider the dispersion of both the TE_{00} and TM_{00} and find all the λ_1 , λ_2 and λ_3 that fulfill both energy conservation and phase-matching condition. The tunability curve is shown in figure(2.18). The vertical dashed lines represents specific cases for which the conversion efficiency η_0 has been evaluated by means of equation 2.6 conveniently adapted to the case of type 1 phase matching. It is worth to noticing that the new η_0 is two order of magnitude higher than in the case of low-contrast waveguides. This is due to the fact that in this second kind of waveguides we are considering a type I phase matching between fundamental modes. The overlap integral between fundamental modes is much larger values when it is evaluated between fundamental modes than higher-order modes, which indeed present some nodes that lower the overall value of the integral.

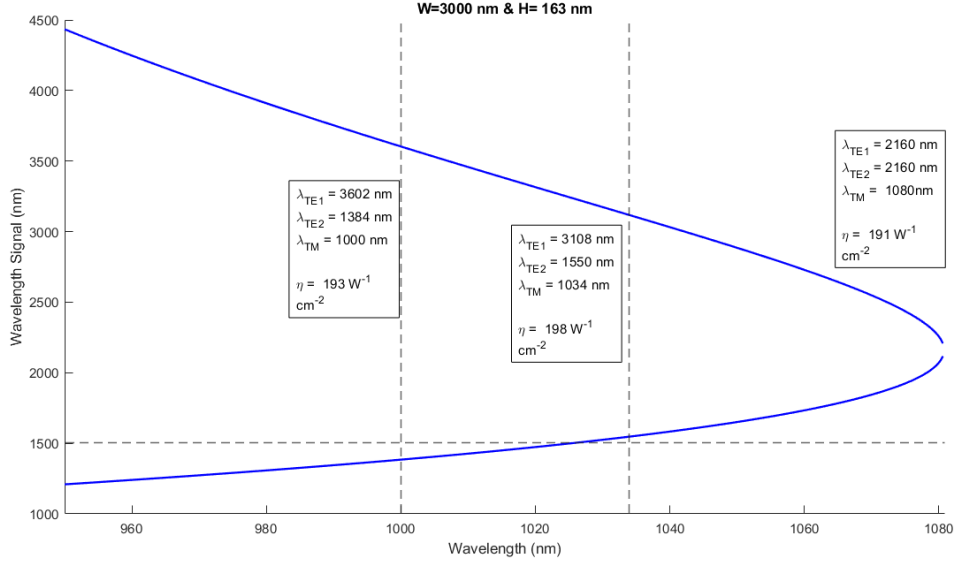


Figure 2.18: Tunability curve of the high-contrast straight waveguide. Dashed vertical lines represent the output wavelengths λ_3 for which η_0 has been evaluated. The horizontal dashed line represents the wavelength below which two photon absorption (TPA) occurs.

2.2.1 Arc-shape waveguide and tunability

Similarly to low-contrast waveguides, I had to consider the different phase matching condition for the arc-shaped parts of the guides. The physical considerations are essentially the same with respect to the previous case, since the material used for the core is again AlGaAs. It is therefore possible to evaluate the tunability of the entire structure by performing a very similar procedure: first I evaluate the momentum mismatches $\Delta\beta$ and $\Delta\beta_{\text{arc}}$ for different ω_1 , ω_2 and $\omega_3 = \omega_1 + \omega_2$. Then I consider a unit cell made of three straight parts and two arcs and I iterate equation (2.9) for a certain number of cells (in this case 5 cells were considered) in order to evaluate the amplitude $|A_{\omega_3}|^2$ as function of λ_1 and λ_2 .

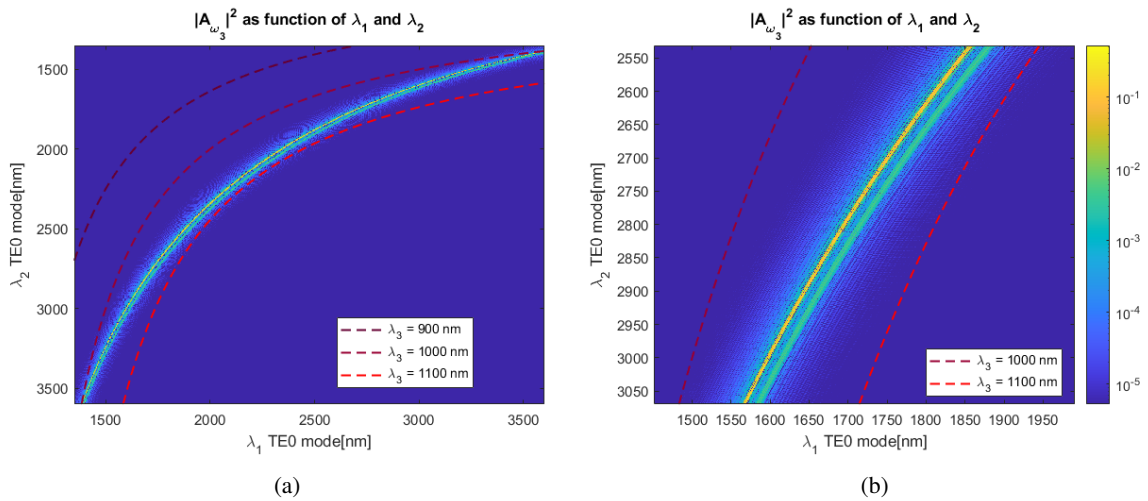


Figure 2.19: a) $|A_{\omega_3}|^2$ in logarithmic scale as function of the input signal λ_1 and the pump λ_2 for a structure composed by 5 unit cells. The dashed colored lines represents the loci of constant λ_3 b) Zoomed image of the previous

Figure (2.19) shows square modulus of the amplitude $|A_{\omega_3}|^2$ of the optical wave at λ_3 as a function of the impinging wavelength at λ_1 and λ_2 . Once more it is possible to appreciate that it exists a region in the λ_1/λ_2 plane for which the intensity of the TM_{00} mode at λ_3 is not vanishing and therefore the entire structure presents its own tunability. In the zoomed image (b) it is possible to appreciate the presence of a double line, meaning that also for this kind of structures is characterized by a double peak in the intensity.

2.2.2 Fabrication of high-contrast waveguides

Since it is not possible to grow epitaxial (Al)GaAs on top of of SiO_2 due to the amorphous nature of the latter, the fabrication of high-contrast waveguides requires a wafer bonding technique between a silicon on insulator wafer and a GaAs wafer on top of which it has been grown the desired epitaxy. Figure (2.20) is a schematic of this technology. First the two wafers are bonded together by means of an adhesive layer of BCB. Next it is necessary to remove the GaAs substrate correctly and the process is carried out via a wet etching technique. In order to do so, it is required to have an etch-stop layer of $Al_{0.8}Ga_{0.2}As$ between the substrate and the desired $Al_{0.18}Ga_{0.82}As$ layer. The substrate of GaAs, which thickness is several hundreds of m is removed by a citric acid solution at high temperature. Citric acid is highly selective on the $Al_{0.8}Ga_{0.2}As$ layer with respect to the GaAs. In order to remove the etch stop layer, whose thickness is of the order of some hundreds of nm, it is used a solution of BOE for few minutes.

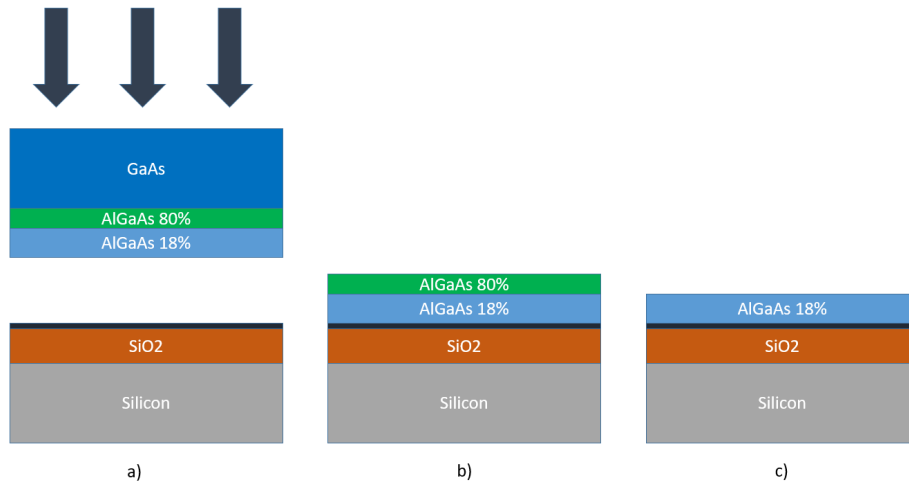


Figure 2.20: Schematic of the fabrication process. a) wafer bonding is performed between a Silicon wafer and a GaAs wafer on top of which it has been grown the desired epitaxy. b) Then the GaAs substrate is removed by a citric acid solution. c) Lastly the etch stop layer of $Al_{0.8}Ga_{0.2}As$ is removed with a BOE solution for few minutes.

Once the substrate is ready, the following step is a lithographic process in order to define the waveguides. Since the width of our ridge waveguides is quite small and it is necessary to have the highest quality of the edges possible, I resorted to electron-beam lithography. In order to do that, first a negative resist MAN2401 is spun over the sample and then the electron-beam lithography is performed. The last process is the ICP-RIE performed with chlorate gasses to etch the $Al_{0.18}Ga_{0.72}As$. Figure(2.21) is a electron microscope picture of a $Al_{0.18}Ga_{0.72}As$ waveguide on top of SiO_2 obtained with this procedure.

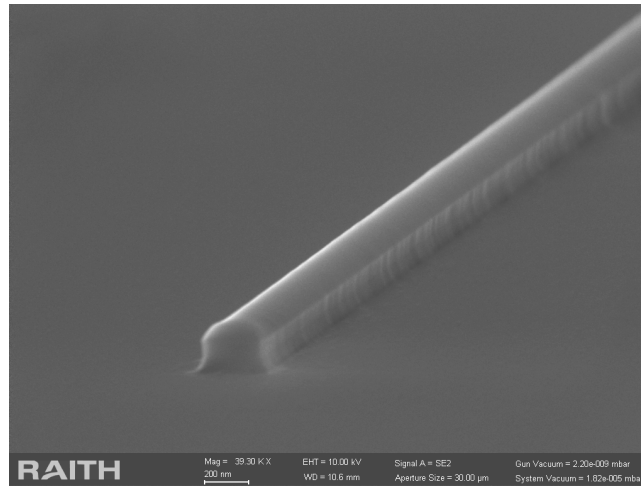


Figure 2.21: Electron microscope picture of a $Al_{0.18}Ga_{0.72}As$ waveguide

2.3 Conclusion

I have designed a slalom shaped waveguide in AlGaAs by means of two different kinds of structures, one low-contrast and one high-contrast, used for the realization of a device that will work in up-conversion. Both waveguides required to be phase matched on a large range of wavelengths in order to have an efficient second-order nonlinear conversion between the interacting modes. However the phase matching condition changes on the curved parts with respect to the straight ones, threatening the tunability of the whole device. It was therefore necessary to consider the tunability of the entire slalom waveguide in order to understand the efficiency of the nonlinear conversion.

For both kind of waveguides it is possible to have an efficient tunability over a wide range of wavelengths. In particular, the low-index waveguides presents a larger core dimensions which should guarantee low loss. On the other hand for this kind of structures it is not possible to achieve a type I phase matching and therefore is necessary to deal with higher order modes. For what concerns the high-contrast waveguides, despite the smaller dimension of the core, it is possible to have a nonlinear interaction between fundamental modes.

This is a great advantage with respect to the previous case for many physical reasons. First of all, a type II phase matching working in down conversion requires to excite a TE_{20} mode, which in general is not trivial and requires some challenge. Moreover I have shown that the nonlinear conversion between fundamental modes is two order of magnitude higher with respect to the one evaluated with higher order modes due to the different geometrical overlap of the modes.

On the other hand, high-contrast waveguides require a wafer bonding technique followed by a wet etching substrate removal that complicates the fabrication process and can affect the quality of the guide. Overall after all this consideration we have decided to work with a high-contrast waveguide for the realization of the device.

In the next period of my stage I will first characterize the effective index of the AlGaAs on SiO_2 platform in order to have a reference on the real values of the indices of the materials. In order to do so, I have designed and fabricate a grating coupler on the platform that I will use to couple a near infrared light. The angle of incidence for which coupling occurs between the free space radiation and the planar waveguide depends on the effective index of the material.

Next, once the real effective index of the material will be characterized, I will fabricate short AlGaAs waveguides correctly phase matched in order characterize the loss of both straight and

arc shaped guides. The values of the loss is essential to determine the maximum length possible for the guide.

To conclude I have shown using numerical simulations the possibility to realize an on-chip integrable tunable device for up-conversion in the mid-IR. The final step will be the realization and the characterization of the slalom-shape waveguide; the comparison of the measurements will be a feedback to understand the effective correspondence with the theory developed in this work.

Chapter 3

Reference articles

1. R.W. Boyd, Nonlinear optics, 3rd ed. Academic(2008)
2. T.suhara, M.Fujumura, Waveguide Nonlinear-optic devices, Springer (2003)
3. C.Autebert et al., Integrated AlGaAs source of highly indistinguishable and energy-time entangled photons, *Optica*, **3**(2), 143 (2016)
4. K.A. Rutkowska et al., Second Harmonic Generation in AlGaAs Nanowaveguides, *Acta Phys. Pol. A* , **120**, P 725 (2011)
5. T. Matsushita et al., Design of zigzag folded inversion-stacked AlGaAs waveguides for ultra-compact wavelength converters, *Optics Express*, **25**(19), 22830, (2017)
6. L. Cai et al., Highly efficient broadband second harmonic generation mediated by mode hybridization and nonlinearity patterning in compact fiber-integrated lithium niobate nanowaveguides, *Sci Rep*, **8**, 12478 (2018)
7. L.Chang et al., Heterogeneously Integrated GaAs Waveguides on Insulator for Efficient Frequency Conversion, *Laser Photonics Rev.*, **12**, 1800149 (2018)
8. J.Haines et al., Mid-Infrared Frequency Generation via Intermodal Difference Frequency Generation in AlGaAs-On-Insulator Waveguides, *Front. Photonics*, **2**,788174 (2021)
9. P.S. Kuo et al. Second-harmonic generation using 4⁺-quasi-phasematching in a GaAs whispering-gallery-mode microcavity, *Nature Comm.* **5**, 3109 (2014).
10. M. Pu et al., Ultra-Efficient and Broadband Nonlinear AlGaAs-on-Insulator Chip for Low-Power Optical Signal Processing, *Laser Photonics rev.*,**12**, 1800111 (2018)
11. I.Roland et al., Second-Harmonic Generation in Suspended AlGaAs Waveguides: A Comparative Study, *Micromachines*, **11**, 229 (2019).
12. R.L. Sutherland, Handbook of Nonlinear Optics 2nd ed. (Marcel Dekker Inc., 2003).
13. T.W. Kim et al., Phase-matched second-harmonic generation in thin rectangular high-indexcontrast AlGaAs waveguides, *Appl. Phys. Express*, **4**(8), 082201 (2011).

